*nanomaterials*

MDPI

*Article*

# Understanding the $CH_4$ Conversion over Metal Dimers from First Principles

**Haihong Meng [1], Bing Han [1], Fengyu Li [1,*], Jingxiang Zhao [2,*] and Zhongfang Chen [3,*]**

[1] School of Physical Science and Technology, Inner Mongolia University, Hohhot 010021, China; dundun_0521@163.com (H.M.); binghan1214@163.com (B.H.)
[2] Key Laboratory of Photonic and Electronic Bandgap Materials, College of Chemistry and Chemical Engineering, Ministry of Education, Harbin Normal University, Harbin 150025, China
[3] Department of Chemistry, University of Puerto Rico, Rio Piedras Campus, San Juan, PR 00931, USA
* Correspondence: fengyuli@imu.edu.cn (F.L.); xjz_hmily@163.com (J.Z.); zhongfangchen@gmail.com (Z.C.)

**Abstract:** Inspired by the advantages of bi-atom catalysts and recent exciting progresses of nanozymes, by means of density functional theory (DFT) computations, we explored the potential of metal dimers embedded in phthalocyanine monolayers ($M_2$-Pc), which mimics the binuclear centers of methane monooxygenase, as catalysts for methane conversion using $H_2O_2$ as an oxidant. In total, 26 transition metal (from group IB to VIIIB) and four main group metal (M = Al, Ga, Sn and Bi) dimers were considered, and two methane conversion routes, namely *O-assisted and *OH-assisted mechanisms were systematically studied. The results show that methane conversion proceeds via an *OH-assisted mechanism on the $Ti_2$-Pc, $Zr_2$-Pc and $Ta_2$-Pc, a combination of *O- and *OH-assisted mechanism on the surface of $Sc_2$-Pc, respectively. Our theoretical work may provide impetus to developing new catalysts for methane conversion and help stimulate further studies on metal dimer catalysts for other catalytic reactions.

**Keywords:** metal dimers; nanozymes; methane conversion; density functional theory



**Citation:** Meng, H.; Han, B.; Li, F.; Zhao, J.; Chen, Z. Understanding the $CH_4$ Conversion over Metal Dimers from First Principles. *Nanomaterials* **2022**, *12*, 1518. https://doi.org//10.3390nano12091518

Academic Editor: Giuseppe Cappelletti

Received: 26 March 2022
Accepted: 27 April 2022
Published: 29 April 2022



## 1. Introduction

Global warming is gaining increasing concern worldwide. Greenhouse gases include carbon dioxide, methane, nitrous oxides, and other gases. According to EPA, carbon dioxide accounted for ca. 80% of all greenhouse gas emissions from human activities in the USA in 2019. Though methane has a lower emission (10%), it is also a major greenhouse gas since its greenhouse effect is 21 to 23 times that of carbon dioxide [1]. Therefore, the effective conversion of methane into value-added chemicals (instead of direct burning) is of both environmental and commercial importance [2–4].

The direct conversion of methane mainly associates with the high C−H bond strength (~434 kJ/mol) in the non-polar and highly symmetric methane [5–8]. In traditional industries, methane is first converted into syngas, then transferred to liquid hydrocarbons by Fischer–Tropsch process, which not only causes waste of resources, but also requires a high equipment maintenance cost [9–14]. Biological enzyme catalysis may be a good alternative since it has the advantages of high product selectivity and mild reaction conditions: compared with the current industrial process, the direct conversion of methane to methanol that occurs in the methane monooxygenase (MMO) from *Methylococcus capsulatus* is much more efficient [15–18]. Due to their high catalytic efficiency, biological enzymes can greatly increase the rate of chemical reactions, saving time and cost. Unfortunately, structural instability and sensitivity to the environment greatly limit their performance in industrial applications. A promising way to conquer such challenges is to mimic the MMO with the binuclear active sites [19–21]. Zeolites such as ZSM-5 are able to form stable binuclear centers (diiron or dicopper) in similar enzymes, and exhibit unprecedented high performance in methane conversion, but their catalytic mechanism and structure–property

relationship remain unclear. The direct conversion of methane at room-temperature and atmospheric pressure is still an unsolved but high-rewarding challenge [22,23].

Nanozymes are a class of nanomaterials with unique enzyme-like properties, which have very similar active sites and catalytic mechanisms to biological enzymes. The first nanozymes were discovered in 2007, since then more than 300 nanomaterials have been found to have enzymatic activity [24–26]. Since "single-atom catalysis" was proposed in 2011, the concept of single-atom nanozymes (SAzymes) has also emerged as a research hotspot [27–30]. Compared with single-atom catalysts, bi-atom catalysts may possess improved catalytic performance [31,32]. For example, Yan et al. showed that Pt dimers embedded in graphene have 17-fold and 45-fold higher catalytic activity for the hydrolytic dehydrogenation of ammonia borane than its corresponding single-atom and nanoparticle counterparts [33]. Li et al. demonstrated that Cu dimers supported on $C_2N$ layers exhibited superior performance for CO oxidation compared to $Cu_1@C_2N$ [34], and showed excellent performance with a small confinement potential of $-0.23$ V for electrochemical $CO_2$ reduction [35]. However, to date, few studies have been reported on the catalytic performance of supported metal dimers for methane conversion. Inspired by the advantages of nanozymes and bi-atom catalysts, we designed a series of supported metal dimer catalysts for methane conversion by mimicking the binuclear centers in biological enzymes based on density functional theory computations.

The two-dimensional (2D) phthalocyanine-based (Pc) catalysts have a high surface area to volume ratio, abundant binding sites for anchoring metal atoms and the ability to prevent these metal atoms from aggregating into clusters. In 2011, Abel et al. [36] successfully prepared FePc complex and characterized the samples using scanning tunneling microscope (STM) at room temperature. Later on, Matsushita et al. [37] synthesized a rectangular phthalocyanine with two adjacent transition metal sites. Since Pc and transition metals are of low-cost, environmentally benign, more readily available than precious metals, the Pc-supported transition metal catalysts can be produced in a low-cost manner. Note that DFT calculations have been widely used to provide guidance in conversion/bonding/adsorption of molecules/clusters and reactions [38,39]. Here, first-principles calculations were conducted to explore the potential of all the 3d, 4d, and 5d non-toxic transition metals and the four main group metal (M = Al, Ga, Sn and Bi) dimers supported on the Pc ($M_2$-Pc) for methane conversion.

## 2. Computational Methods

All the computations were carried out by spin-polarized density functional theory (DFT) calculations including van der Waals (vdW) corrections (DFT-D2) [40], as implemented in Vienna Ab initio Simulation Package (VASP) using the projector augmented wave (PAW) method [41]. The generalized gradient approximation (GGA) with the Perdew–Burke–Ernzerhof (PBE) exchange-correlation functional was adopted [42]. The energy cutoff for the plane-wave basis set was chosen as 550 eV, the systemic energy tolerance and the remaining total force were set as $1 \times 10^{-5}$ eV and 0.01 eV Å$^{-1}$, respectively. The Brillouin zone was sampled with a $5 \times 5 \times 1$ k-points grid of the Monkhorst–Pack scheme [43] for geometry optimization, and a denser k-mesh of $15 \times 15 \times 1$ for electronic structure computations. To avoid interactions between periodic images, a vacuum space of 15 Å was used in the perpendicular direction of the 2D layer. The reaction energy barriers were estimated using the climbing-image nudged elastic band (CI-NEB) method [44,45], and the transition states were obtained by relaxing the force below 0.05 eV/Å. The entropic effects were not included in estimating reaction barriers. The binding energy ($E_b$) of a metal atom was computed from the following equation.

$$E_b = (E_{tot} - E_{sub} - 2 * E_M)/2$$

where $E_{tot}$, $E_{sub}$, and $E_M$ represent the total energy of the complex of substrate and metal atoms, the energy of the substrate, and the energy of a free $M$ atom, respectively. According

to this definition, a more negative $E_b$ value indicates a higher thermodynamic stability. The adsorption energy ($E_{ads}$) of an adsorbate was computed according to the following equation:

$$E_{ads} = E_{tot} - E_{cat} - E_{adsorbate}$$

where the $E_{tot}$ is the total energy of an adsorbate adsorbed on the catalyst, $E_{cat}$ and $E_{adsorbate}$ represent the energies of the catalyst and a free adsorbate, respectively. The reaction energy ($E_{rea}$) and activity energy barrier ($E_{act}$) were calculated using the following expressions:

$$E_{rec} = E_{FS} - E_{IS}$$

$$E_{act} = E_{TS} - E_{IS}$$

in which $E_{FS}$, $E_{IS}$, and $E_{TS}$ denote the energies of the final, initial, and transition states, respectively. The reaction mechanism can also be effectively modeled by ab initio molecular dynamics (AIMD) simulations at specific temperatures [46].

## 3. Results and Discussion

This work describes our efforts to study the catalytic activity of $M_2$-Pc on the conversion of methane. In this paper, we use $H_2O_2$ as the oxidant, because its reaction by-product is only water, which is a green catalyst [47]. Moreover, $H_2O_2$ has been widely used as an oxidant to study the conversion of methane [48–52]. The $CH_4$ oxidation with $H_2O_2$ via both *OH- and *O-assisted mechanisms was investigated in detail [48].

### *3.1. Geometric Structure and Stability of $M_2$-Pc*

First, the geometric structure of the Pc monolayer was optimized, and the lattice parameters *a* and *b* in the Pc monolayer of 14.13 Å were used. As shown in Figure S1a, the unique cavity structure of Pc can provide ideal anchoring sites for the metal atoms to be connected, to four isoindole rings, preventing their migrating and aggregating. The computed energy band gap of Pc sheet is 0.94 eV (in Figure S1b,c). The geometric structures and related information of the optimized $M_2$-Pc are shown in Figure S2 and Table S1. Obviously, due to the different radii of the metal atoms, the structures of $M_2$-Pc are slightly different. The anchored metal atoms with smaller atomic radii form an in-plane configuration in the Pc cavity (Al, Mn, Fe, Co, Ni, Cu, Ga, Ru, Rh, Re, Os, and Ir), while others with larger atomic radii are pulled out of the Pc plane and lead to a buckled structure.

To confirm the stability of metal dimers embedded in the Pc sheet, the binding energy ($E_b$) was calculated. Meanwhile, the corresponding metal bulk cohesive energy ($E_{bulk}$) were compared (Table S1), which are less negative than $E_b$, indicating that the interaction between the metal atoms and Pc monolayer is very strong, i.e., the anchoring of metal dimers on the Pc has strong coupling and good stability. We also performed AIMD simulations of the $Ag_2$-Pc monolayer, whose binding energy is the least favorable (−4.13 eV) among the considered systems (−13.47~−4.13 eV), and found that the monolayer structure was well kept during 5 ps's annealing at 300, 800, 1000, 1300, and 1500 K, respectively, and bond breakage occurred at 1500 K (Figure S3). Therefore, all the models in our work have high thermal stability, and in the next section, we will study the catalytic mechanism for methane conversion on these $M_2$-Pc catalysts.

### *3.2. Decomposition of $H_2O_2$ on $M_2$-Pc*

Since the adsorption and dissociation of oxidants are important in methane oxidation, we considered both side-on and end-on configurations of the $H_2O_2$ adsorption (Figure S4) on the examined 30 $M_2$-Pc, including 26 transition metals from IB to group VIIIB and four main group metals (M = Al, Ga, Sn and Bi).

Upon adsorption, $H_2O_2$ will spontaneously decompose on the surface of the nine $M_2$-Pc (M = Sc, Ti, V, Y, Zr, Nb, Hf, Ta, and W), all of which are highly exothermic (as shown in Table S2). As shown in Figure 1, $H_2O_2$ can be dissociated when the electronic state of

the embedded atoms is a semi-occupied state. Among them, a $H_2O_2$ is spontaneously decompose into a $H_2O$ and an adsorbed oxygen ($H_2O_2 \rightarrow *O + *H_2O$) on the $Nb_2$-Pc with the energy release of −6.08 eV, and into two adsorbed hydroxy groups ($H_2O_2 \rightarrow 2 * OH$) on the five $M_2$-Pc (M = Ti, V, Y, Hf, and Ta with the exothermic energy of −7.51, −6.70, −5.03, −8.71, and −9.04 eV, respectively), while into either a water molecule and an atomic oxygen (by releasing the heat of −3.75, −6.29, and −4.78 eV, respectively), or two OH species (by releasing the heat of −5.19, −8.16, and −7.41 eV, respectively) on the $Sc_2$-Pc, $Zr_2$-Pc, and $W_2$-Pc. All the surface-adsorbed oxo species (*O) occupy the bridge position of the metal dimers. We also examined the magnetic moments and Bader charges on the metal atoms of these nine $M_2$-Pc monolayers (M = Sc, Ti, V, Y, Zr, Nb, Hf, Ta, W) (Table S3), among which the $Sc_2$-Pc, $Ta_2$-Pc, $Y_2$-Pc, and $W_2$-Pc have spin states in singlet, the $Nb_2$-Pc, $Ti_2$-Pc, $Zr_2$-Pc, and $Hf_2$-Pc are triplet, while $V_2$-Pc is in quintet spin state. According to the dissociation structure and energy, $H_2O_2$ dissociation on these nine catalysts (Figure S5 and Table S2) are much more exothermic than the previously reported dissociation reaction of $H_2O_2$ on Pd(111) and Au/Pd(111) surfaces (−1.76 and −1.58 eV for two adsorbed hydroxy groups, and −2.27 and −2.06 eV for absorbed oxygen) [53]. Therefore, it is believed that the decomposition of $H_2O_2$ on these nine catalysts is likely to occur under environmental conditions. Unexpectedly, $Fe_2$ and $Cu_2$ metal centers, very common active center in biological systems and some biomimetic compounds [54], cannot decompose $H_2O_2$ to form reactive intermediates on Pc sheet.

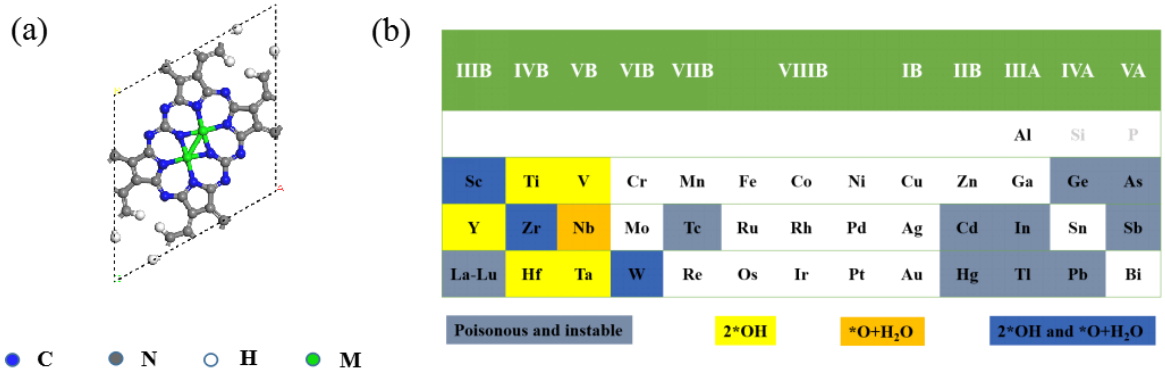


**Figure 1.** (**a**) Top view of $M_2$-Pc sheet. (**b**) The metals examined in this work. The poisonous metals were indicated in gray; the metals assist $H_2O_2$ decomposition into 2*OH or *O and $H_2O$ are highlighted in yellow and orange, respectively; the metals could decompose $H_2O_2$ into either 2*OH or *O and $H_2O$ are represented in blue; metals in white cannot spontaneously decompose $H_2O_2$.

### *3.3. Catalytic Conversion of Methane on the $M_2$-Pc*

Previous theoretical studies by Yoo et al. [53] showed that when *OH and *O species exist on the surface, the activation energy barrier of the C−H bond on the precious metal will be decreased [48,55,56]. Based on the spontaneous decomposition of $H_2O_2$ on $M_2$-Pc, two mechanisms of $CH_4$ conversion will be examined: the *OH-assisted mechanism on $Sc_2$-Pc, $Ti_2$-Pc, $V_2$-Pc, $Y_2$-Pc, $Zr_2$-Pc, $Hf_2$-Pc, $Ta_2$-Pc, and $W_2$-Pc, the *O-assisted mechanism on $Nb_2$-Pc, $Sc_2$-Pc, $Zr_2$-Pc, and $W_2$-Pc.

#### 3.3.1. OH-Assisted Methane Conversion

We first examined the methane conversion over $Sc_2$-Pc, $Ti_2$-Pc, $V_2$-Pc, $Y_2$-Pc, $Zr_2$-Pc, $Hf_2$-Pc, $Ta_2$-Pc, and $W_2$-Pc via *OH-assisted mechanism. The two quenching reactions of *OH, namely the disproportionation of two OH groups to $H_2O$ and O ($2(*OH) \rightarrow *O + *H_2O$) [57] and the self-reaction of $H_2O_2$ ($H_2O_2 + 2(*OH) \rightarrow O_2 + 2H_2O$) [58], will result in a low reaction efficiency, thus the quenching reactions were investigated before the calculation.

The disproportionation of two *OH groups to $H_2O$ and *O on the $Ti_2$-Pc, $V_2$-Pc, $Y_2$-Pc, $Hf_2$-Pc, and $Ta_2$-Pc were firstly evaluated. As shown in Table S4, the reaction on $Y_2$-Pc, $Hf_2$-Pc, and $Ta_2$-Pc are difficult (Gibbs free energies are 1.83, 1.72, and 1.63 eV, respectively),

in comparison, the free energy change on $Ti_2$-Pc and $V_2$-Pc are both less than 1 eV. However, the energy barriers on $Ti_2$-Pc and $V_2$-Pc are as high as 1.95 and 2.59 eV, respectively (Figure S6), indicating that the reaction is also difficult to proceed on these two catalysts. Though on $Sc_2$-Pc, $Zr_2$-Pc, and $W_2$-Pc catalysts, the decomposition of $H_2O_2$ into a $H_2O$ and an adsorbed oxygen are more energy-efficient than the splitting into two *OH, considering that the splitting into two *OH on these three catalysts is spontaneous, we also calculated the methane conversion via *OH-assisted mechanism on these three catalyst surfaces.

The formation of $O_2$ is also a competitive reaction, which means that $H_2O_2$ may become its own scavengers. The energy parameters for the self-reaction on the six $M_2$-Pc (M = Ti, V, Zr, Sc, Y, and Hf) are given in Table S5, the rather high Gibbs free energies for the reaction on the $Ti_2$-Pc, $V_2$-Pc, and $Zr_2$-Pc (2.61, 2.69, and 3.08 eV, respectively) indicate that the self-reaction on these three catalysts is not thermodynamically favorable. No matter what initial structure is built on the $Ta_2$-Pc and $W_2$-Pc, they will become two adsorbed hydroxy groups after relaxation, i.e., the reaction will not proceed on either $Ta_2$-Pc or $W_2$-Pc. The calculated reaction energies over the $Sc_2$-Pc, $Y_2$-Pc, and $Hf_2$-Pc are 0.54, 0.65, and −0.18 eV, respectively; however, the activation energy barriers are 2.27, 1.66, and 1.36 eV, respectively (Figure S7), which means that the *OH is also difficult to quench on these three catalysts.

The above results showed that *OH will not be quenched on the eight catalysts examined in this section. Based on this finding, we investigated the methane conversion reaction via *OH-assisted mechanism.

First, $CH_4$ is weakly adsorbed on the catalyst covered by OH, and the C−M bond lengths are 2.59, 2.42, 2.37, 2.81, 2.51, 2.45, 2.64, and 2.42 Å on the $Sc_2$-Pc, $Ti_2$-Pc, $V_2$-Pc, $Y_2$-Pc, $Zr_2$-Pc, $Ta_2$-Pc, $W_2$-Pc, and $Hf_2$-Pc, respectively. The adsorption energies are −0.15, −0.53, −0.52, −0.41, −0.49, −0.61, 0.28, and −0.22 eV, respectively. The reaction energies of surface *OH groups attracting H from $CH_4$ are 0.76, 0.81, 0.59, 0.95, −0.14, 0.58, and 0.83 eV on $Sc_2$-Pc, $Ti_2$-Pc, $V_2$-Pc, $Y_2$-Pc, $Zr_2$-Pc, $Ta_2$-Pc, and $Hf_2$-Pc, respectively; the corresponding activation energy barriers are 1.09, 0.85, 1.41, 1.35, 0.86, 0.62, and 1.22 eV. The reaction of extracting H from $CH_4$ on the $W_2$-Pc is not considered because its repulsiveness to $CH_4$ (Figure S8). These analyses suggested that $Ti_2$-Pc, $Zr_2$-Pc, and $Ta_2$-Pc can catalyze the C-H breakage due to favorable reaction energies and relatively mall activation barriers (0.85, 0.86 and 0.62 eV). Note that though the activation barrier on $Sc_2$-Pc is slightly high (1.09 eV), considering that the O-assisted methane conversion on this catalyst benefits from the assistance of *OH (see Section 3.3.2), we also investigated the the *OH-assisted mechanism on $Sc_2$-Pc. Thus, four catalysts which are feasible to break the C-H bonds, namely, $Sc_2$-Pc, $Ti_2$-Pc, $Zr_2$-Pc, and $Ta_2$-Pc, will be further investigated.

Then, we calculated the subsequent reactions over $Sc_2$-Pc, $Ti_2$-Pc, $Zr_2$-Pc, and $Ta_2$-Pc. Figure 2a–d summarizes the corresponding potential energy profile and the optimized geometries along the reaction path on these four $M_2$-Pc. After the cleavage of the C−H bond, $CH_3$ and $H_2O$ are adsorbed on the four catalyst surfaces. Next, the desorption of $*CH_3$, the desorption of $*H_2O$, and the reaction with OH in the solution to generate $CH_3OH$ were considered, respectively. The best path for all these four catalysts is to react with OH in the solution. Note that $*CH_3$ will react with ·OH in the solution to form $CH_3OH$ on $Sc_2$-Pc and $Ti_2$-Pc, the reaction proceeds spontaneously on $Sc_2$-Pc, and the energy barrier on $Ti_2$-Pc is only 0.08 eV. While on $Zr_2$-Pc and $Ta_2$-Pc, OH will combine with the H atom of *OH to generate $H_2O$ instead of reacting with $*CH_3$ (this process occurs spontaneously on both catalysts). After desorbing $H_2O$, $*CH_3$, and *OH will remain on the surface. Unexpectedly, on both $Zr_2$-Pc and $Ta_2$-Pc catalysts, $*CH_3$ will not combine with *OH on the surface to form $CH_3OH$, but will combine with ·OH in the solution to generate $CH_3OH$ (the energy barriers are 0.84 and 0.08 eV, respectively, as shown in Figure 2c,d).

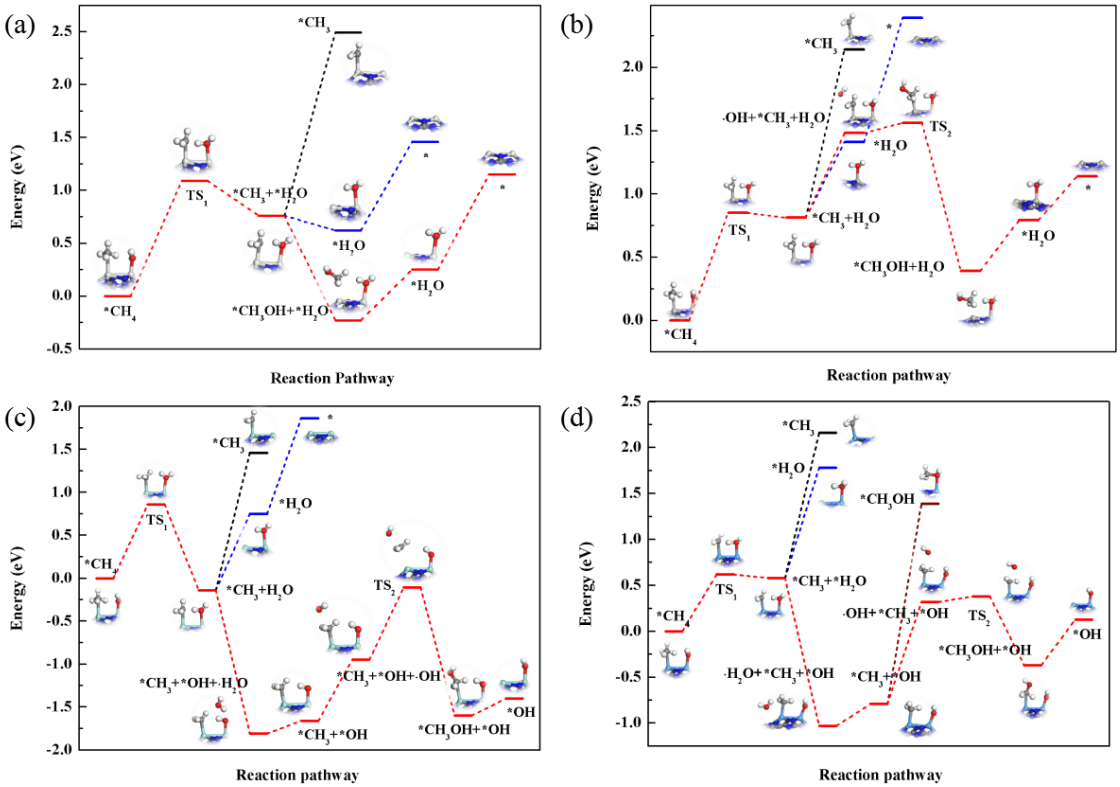


**Figure 2.** Reaction pathway of *OH-assisted $CH_4$ decomposition on the $Sc_2$-Pc (**a**), $Ti_2$-Pc (**b**), $Zr_2$-Pc (**c**), and $Ta_2$-Pc (**d**) monolayers. Blue, black, and red lines represent the reaction paths for *$CH_3$ desorption, *$H_2O$ desorption, and the reaction with OH in the solution, respectively.

To summarize, we identified that four catalysts, namely, $Sc_2$-Pc, $Ti_2$-Pc, $Zr_2$-Pc, and $Ta_2$-Pc, show high $CH_4$ conversion activity with the assistance of *OH. The rate-limiting steps of $Sc_2$-Pc, $Ti_2$-Pc, and $Zr_2$-Pc are the cleavage of the first C−H bond, with energy barriers of 1.09, 0.85, and 0.86 eV, respectively. The rate-limiting steps of $Ta_2$-Pc is the extraction of ·OH in the solution, with energy barriers of 1.11 eV.

### 3.3.2. O-Assisted Methane Conversion

Then we examined *O-assisted methane conversion on the $Nb_2$-Pc, $W_2$-Pc, $Zr_2$- Pc, and $Sc_2$-Pc catalysts. The adsorption energies of *$H_2O$ on these four $M_2$-Pc are 0.27, 0.13, 0.21, and 0.31 eV, respectively, indicating the feasibility to desorb *$H_2O$ from these slabs to form O-adsorbed catalysts. According to previous studies, the C−H bond cleavage may occur via either a surface-stabilized ($*O + CH_4 \rightarrow *OH + *CH_3$) or a radical-like mechanism ($*O + CH_4 \rightarrow *OH + \cdot CH_3$) [59,60]. Figure S9 shows the energy diagram of methane conversion on these four *O-adsorbed catalysts following the surface-stabilized or radical-like mechanism, and the competition reaction pathway of the *$CH_3$ dehydrogenation is also considered ($*CH_3 + *OH \rightarrow *CH_2 + *H_2O$). In contrast to the quintet state of Fe(IV)(oxo) in Fe(IV)O/MOF-74 [61], the M-O-M moiety (M = Sc, Zr, Nb, W) is singlet in the ground state, since the magnetic moment on either M or O is zero. Accordingly, the oxidation state of O and Sc/Zr/Nb/W could be assigned as −2 and +3/+4/+4/+4, respectively, which is quantitatively in line with our Bader charge analysis (Table S6). Notably, the spin state of $Nb_2$-Pc and $Zr_2$-Pc switches from the triplet to the singlet when forming M-O-M moiety, agreeing well with our recent theoretical observations in metal dimer-related catalysis [62]. The partial density of states (PDOS) of $CH_4$ adsorption on M-O-M moiety (Figure S10) shows that there is orbital hybridization between M-O-M and $CH_4$.

Among these examined catalysts, *O-assisted conversion of methane is energetically more favorable on the $Sc_2$-Pc monolayer through a surface-stabilized mechanism (Figure S9). This is different from the traditional single-site catalyst, which prefers the

free radical mechanism [60–65]. The potential energy profile and the reaction path of *O-assisted methane C−H bond cleavage on the $Sc_2$-Pc surface are illustrated in Figure 3, in which the C−H bond activation is found as the rate-determining step for the first methanol formation. The reaction begins with the adsorption of $CH_4$, which is physically adsorbed on the O-preadsorbed $Sc_2$-Pc through van der Waals interaction as the initial state with the adsorption energy of −0.09 eV, where the C−H bond length is 1.10 Å, slightly longer than that in the free $CH_4$ molecule (1.07 Å), and the distance between O and H is 1.84 Å. In the transition state, the distance between C and H is elongated to 1.47 Å, and the distance between O and H is shortened to 1.21 Å, both of which are between the initial state and the final state. In the final state, *OH and *$CH_3$ will form one Sc−C (bond distance of 2.25 Å) and two Sc−O bonds (bond lengths 1.97 and 2.37 Å) on surface. In other words, the *O-assisted methane activation on the $Sc_2$-Pc catalyst follows the surface-stabilized mechanism, and the energy barrier for activation of the first C−H bond is 0.63 eV, which is much lower than the *O-assisted Au (111) surface (1.33 eV) [53].

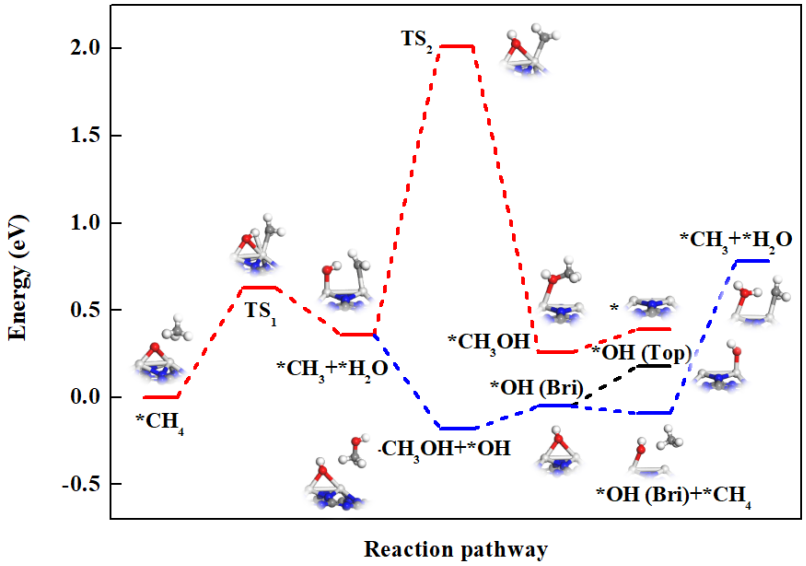


**Figure 3.** Reaction pathway of *O-assisted $CH_4$ decomposition on the $Sc_2$-Pc monolayer. Blue, black, and red lines represent the three paths of *$CH_3$ reacting with *OH, *$CH_3$ reacting with ·OH in solution, and the migration of *OH from bridge to top site, respectively.

After the C-H bond cleavage on $Sc_2$-Pc, the position of *O is transferred from the bridge site of two Sc atoms to the top of one Sc atom, and *$CH_3$ is adsorbed on the other Sc atom. Unlike single-site active center catalysts, bi-atom active centers increase the adsorption strength of the intermediates, thereby preventing the combination of *$CH_3$ and *OH, which can be seen from the very high energy barrier (1.65 eV) in Figure 3.

We also considered that *$CH_3$ reacts with ·OH in the solution to form *$CH_3OH$. This reaction proceeds spontaneously (the initial state structure and the final state structure are shown in Figure S11) by releasing energy of 0.54 eV (the blue line in Figure 3). The desorption of *$CH_3OH$ requires 0.13 eV of energy. After desorbing $CH_3OH$, *OH remains being adsorbed on the surface occupying the bridge position of Sc dimers. Subsequently, we investigated two reaction paths: *OH moves to the top site of Ta atom, and *OH on the bridge position continues to activate $CH_4$. As shown in Figure 3, the C−H bond cleavage assisted by the *OH on the bridge site is endothermic by 0.87 eV, while the migration of the *OH on the bridge site to the top site is slightly endothermic by 0.23 eV. Therefore, the *OH prefers moving to the top site, and the subsequent reaction is the same as discussed in Section 3.3.1. Noted that the active site motif for $H_2O_2$-converting methane is M-O-M (where M is a metal center), different from the biological MMOs containing binuclear Fe

centers for the oxidation of $CH_4$ to $CH_3OH$ by $O_2$, where the reaction involves the formation of a pair of highly active iron(IV)oxo groups in a "diamond core" arrangement [61].

Note that the DFT self-interaction errors can have significant effects on the reactivity of high-valent Fe species during the oxidation of methane in metal-organic frameworks [66]. Thus, we tested the reaction of the first C–H bond cleavage using the HSE06 functional [67] and compared with the PBE result, $Ti_2$-Pc was taken as a representative due to its best catalytic performance among the catalysts examined in this work. We found that reaction barriers (0.84 vs 0.85 eV) and reaction energies (0.78 vs 0.81 eV) are very close from the two methods (Figure S12). Thus, we conjecture that PBE results are reliable for our systems, and we adopted PBE functional through our calculations.

## 4. Conclusions

To sum up, we designed low-cost bi-atom ($M_2$-Pc) catalysts for $CH_4$ conversion using a two-dimensional material Pc to support the metal dimers. Two methane conversion routes, namely *O-assisted and *OH-assisted mechanisms, over $M_2$-Pc were systematically studied by means of density functional theory computations. Our computations identified four high-performance catalysts for methane conversion: the $Sc_2$-Pc surface following a combined *O-assisted and *OH-assisted mechanism with the C−H bond breaking energy barrier of 0.63 eV, and $Ti_2$-Pc, $Zr_2$-Pc, and $Ta_2$-Pc following *OH-assisted mechanism with energy barriers of 0.85, 0.86, and 1.11 eV, respectively, all these activation barriers are lower than that on the Au(111) surface (1.33 eV) [53]. This work clearly demonstrated that the $M_2$-Pc monolayers can serve as low-cost and efficient bi-atom catalysts for methane conversion, which not only enrich the family of bi-atom catalysts, but also provides new strategy to design effective bi-atom catalysts for methane conversion and related reactions.

**Supplementary Materials:** The Supporting Information is available free of charge at https://www.mdpi.com/article/10.3390/nano12091518/s1. Table S1. The lattice parameters ($a/b$, in Å) of $M_2$-Pc catalysts, their corresponding bond lengths (the bond lengths of metal to metal, metal to nitrogen, $d_{M-M}$, $d_{M-N}$, $d_{M-Nc}$, where Nc represents the N atom adjacent to the C atom, in Å), and the binding energy ($E_b$, in eV) of metal dimer anchoring at Pc monolayer, as well as the cohesive energy ($E_{bulk}$, in eV) of metal in bulk, Table S2. (a) The reaction energy for $H_2O_2$ dissociation into $*O + H_2O$ on $M_2$-Pc (M = Sc, Zr, Nb, W), bond lengths ($d_{M1-O}/d_{M2-O}$, in Å) (M1 = M2 = M), as well as the $H_2O$ binding energies ($E_{ads\ (H2O)}$, eV), (b) The reaction energy for $H_2O_2$ dissociation into $*OH + *OH$ on $M_2$-Pc (M = Sc, Ti, V, Y, Zr, Hf, Ta, W), as well as the bond lengths ($d_{M1-O}/d_{M2-O}$, $d_{O1-O2}$, $d_{O1-H}/d_{O2-H}$, Å) (M1 = M2 = M), O1 and O2 represent the two O atoms bonded to M1 and M2, respectively, Table S3. The total magnetic moments and magnetic moment (in $\mu$B) of two metal atoms of $M_2$-Pc (M = Sc, Ti, V, Y, Zr, Nb, Hf, Ta, W) (structures as shown in Figure S2), and the Bader charge (q, in |e|) of the two atoms. Table S4. The calculated zero-point energy, entropy, and free energy change of the reaction of the abstraction of a hydrogen from one of the *OH groups to the formation of water and oxo species ($*OH + *OH \rightarrow *O + H_2O$) on $M_2$-Pc (M = Ti, V, Y, Hf, Ta), Table S5. The calculated zero-point energy, entropy, and free energy change of the self-reaction of $H_2O_2$ ($2*OH + H_2O_2 \rightarrow O_2 + 2H_2O$) on $M_2$-Pc (M = Sc, Ti, V, Y, Zr, Hf) Table S6. The partial charges of O (O) and M ($M_1/M_2$) for $M_1$-O-$M_2$ (in $q$) (M1 = M2 = Sc, Zr, Nb, W). Values were obtained from Bader charge analysis, Figure S1. Top and side view of the structure of Pc in a 2 × 2 × 1 supercell (a), and its band structure (b) and projected density of state (DOS) (c). The Fermi lever is set to zero, Figure S2. Top and side views of the optimized $M_2$-Pc monolayers, Figure S3. The energy evolution with time progress of the 5 ps MD simulation of the $Ag_2$-Pc at 300 K, 800, 1000, 1300, and 1500 K, as well as the snapshot of structure at the end of 5 ps, respectively, Figure S4. Two adsorption configurations of $H_2O_2$ on the $M_2$-Pc, Figure S5. The structures of spontaneously dissociated $H_2O_2$ on the $M_2$-Pc monolayers, Figure S6. Transformation process of *OH + *OH → *O + $H_2O$ on $Ti_2$-Pc (a) and $V_2$-Pc (b) surfaces. The inset was the atomic structure model of each step, Figure S7. Transformation process of $H_2O_2$ + 2(*OH) → $O_2$ + $2H_2O$ on $Sc_2$-Pc, $Y_2$-Pc and $Hf_2$-Pc surface. The inset was the atomic structure model of each step, Figure S8. The initial state structure (a) and the final state structure (b) of methane adsorption on $W_2$-Pc surface, Figure S9. The corresponding energy profile of methane conversion via *O-assisted mechanism, Figure S10. Partial density of states (PDOS) of $CH_4$ adsorption on M-O-M moiety. The Fermi level was set to zero, Figure S11. The initial state structure (a) and the final state structure (b) of

the reaction between *$CH_3$ and OH in solution on $Sc_2$-Pc, Figure S12. Energy diagram of the C−H bond cleavage on $Ti_2$-Pc surface calculated by PEB and HSE06 functional.

**Author Contributions:** The study was planned and designed by F.L., J.Z. and Z.C.; First-principles calculations were performed by H.M. and B.H; The manuscript was prepared by H.M., B.H., F.L and Z.C.; J.Z. discussed the results and commented on the manuscript together. All authors have read and agreed to the published version of the manuscript.

**Funding:** This work was financially supported by the National Natural Science Foundation of China (11704203, 11964024), the "Grassland Talents" project of Inner Mongolia autonomous region (12000-12102613), and the Young Scientific Talent Development Project of Inner Mongolia University (10000-21221505), and in USA by NSF-CREST Center for Innovation, Research and Education in Environmental Nanotechnology (CIRE2N) (Grant Number HRD-1736093). The authors gratefully acknowledge the computational support from Beijing PARATEAR.

**Institutional Review Board Statement:** Not applicable.

**Informed Consent Statement:** Not applicable.

**Data Availability Statement:** The data presented in this study are available upon reasonable request from the corresponding authors.

**Conflicts of Interest:** The authors declare no conflict of interest.

## References

1. Yang, Z.; Grace, J.R.; Lim, J.C.; Zhang, L. Combustion of Low-Concentration Coal Bed Methane in a Fluidized Bed. *Energy Fuels* **2011**, *25*, 975–980. [CrossRef]
2. Sushkevich, V.L.; Palagin, D.; Ranocchiari, M.; Van Bokhoven, J.A. Selective Anaerobic Oxidation of Methane Enables Direct Synthesis of Methanol. *Science* **2017**, *356*, 523–527. [CrossRef] [PubMed]
3. Yuan, J.; Zhang, W.; Li, X.; Yang, J. A High Performance Catalyst for Methane Conversion to Methanol: Graphene Supported Single Atom Co. *Chem. Commun.* **2018**, *54*, 2284–2287. [CrossRef] [PubMed]
4. Tang, P.; Zhu, Q.; Wu, Z.; Ma, D. Methane Activation: The Past and Future. *Energy Environ. Sci.* **2014**, *7*, 2580–2591. [CrossRef]
5. Narsimhan, K.; Iyoki, K.; Dinh, K.; Román-Leshkov, Y. Catalytic Oxidation of Methane into Methanol over Copper-Exchanged Zeolites with Oxygen at Low Temperature. *ACS Cent. Sci.* **2016**, *2*, 424–429. [CrossRef] [PubMed]
6. Guo, X.; Fang, G.; Li, G.; Ma, H.; Fan, H.; Yu, L.; Ma, C.; Wu, X.; Deng, D.; Wei, M.; et al. Direct, Nonoxidative Conversion of Methane to Ethylene, Aromatics, and Hydrogen. *Science* **2014**, *344*, 616–619. [CrossRef]
7. Kwon, Y.; Kim, T.Y.; Kwon, G.; Yi, J.; Lee, H. Selective Activation of Methane on Single-Atom Catalyst of Rhodium Dispersed on Zirconia for Direct Conversion. *J. Am. Chem. Soc.* **2017**, *139*, 17694–17699. [CrossRef] [PubMed]
8. Holmen, A. Direct Conversion of Methane to Fuels and Chemicals. *Catal. Today* **2009**, *142*, 2–8. [CrossRef]
9. Jin, D.; Zhu, B.; Hou, Z.; Fei, J.; Lou, H.; Zheng, X. Dimethyl Ether Synthesis via Methanol and Syngas over Rare Earth Metals Modified Zeolite Y and Dual Cu–Mn–Zn Catalysts. *Fuel* **2007**, *86*, 2707–2713. [CrossRef]
10. Wang, B.; Albarracín-Suazo, S.; Pagán-Torres, Y.; Nikolla, E. Advances in Methane Conversion Processes. *Catal. Today* **2017**, *285*, 147–158. [CrossRef]
11. Luo, J.Z.; Yu, Z.L.; Ng, C.F.; Au, C.T. $CO_2/CH_4$ Reforming over Ni–$La_2O_3$/5A: An Investigation on Carbon Deposition and Reaction Steps. *J. Catal.* **2000**, *194*, 198–210. [CrossRef]
12. Tang, S.; Ji, L.; Lin, J.; Zeng, H.C.; Tan, K.L.; Li, K. $CO_2$ Reforming of Methane to Synthesis Gas over Sol–Gel-made Ni/$\gamma$-$Al_2O_3$ Catalysts from Organometallic Precursors. *J. Catal.* **2000**, *194*, 424–430. [CrossRef]
13. McFarland, E. Unconventional Chemistry for Unconventional Natural Gas. *Science* **2012**, *338*, 340–342. [CrossRef]
14. Da Silva, M.J. Synthesis of Methanol from Methane: Challenges and Advances on the Multi-Step (Syngas) and One-Step Routes (DMTM). *Fuel Process. Technol.* **2016**, *145*, 42–61. [CrossRef]
15. Schroder, D.; Fiedler, A.; Hrusak, J.; Schwarz, H. Experimental and Theoretical Studies toward a Characterization of Conceivable Intermediates Involved in the Gas-Phase Oxidation of Methane by Bare $FeO^+$. Generation of Four Distinguishable $[Fe,C,H4,O]^+$ Isomers. *J. Am. Chem. Soc.* **1992**, *114*, 1215–1222. [CrossRef]
16. Chen, Y.-M.; Clemmer, D.E.; Armentrout, P.B. Conversion of $CH_4$ to $CH_3OH$: Reactions of $CoO^+$ with $CH_4$ and $D_2$, $Co^+$ with $CH_3OD$ and $D_2O$, and $Co^+(CH_3OD)$ with Xe. *J. Am. Chem. Soc.* **1994**, *116*, 7815–7826. [CrossRef]
17. Lieberman, R.L.; Rosenzweig, A.C. Crystal Structure of a Membrane-Bound Metalloenzyme that Catalyses the Biological Oxidation of Methane. *Nature* **2005**, *434*, 177–182. [CrossRef]
18. Hakemian, A.S.; Rosenzweig, A.C. The Biochemistry of Methane Oxidation. *Annu. Rev. Biochem.* **2007**, *76*, 223–241. [CrossRef]
19. Rosenzweig, A.C.; Frederick, C.A.; Lippard, S.J.; Nordlund, P. Crystal Structure of A Bacterial Non-Haem Iron Hydroxylase that Catalyses the Biological Oxidation of Methane. *Nature* **1993**, *366*, 537–543. [CrossRef]
20. Lipscomb, J.D. Biochemistry of the Soluble Methane Monooxygenase. *Annu. Rev. Microbiol.* **1994**, *48*, 371–399. [CrossRef]

21. Colby, J.; Stirling, D.I.; Dalton, H. The Soluble Methane Mono-Oxygenase of *Methylococcus Capsulatus* (Bath). Its Ability to Oxygenate n-Alkanes, n-Alkenes, Ethers, and Alicyclic, Aromatic and Heterocyclic Compounds. *Biochem. J.* **1977**, *165*, 395–402. [CrossRef] [PubMed]
22. Balasubramanian, R.; Smith, S.M.; Rawat, S.; Yatsunyk, L.A.; Stemmler, T.L.; Rosenzweig, A.C. Oxidation of Methane by a Biological Dicopper Centre. *Nature* **2010**, *465*, 115–119. [CrossRef]
23. Narsimhan, K.; Michaelis, V.; Mathies, G.; Gunther, M.; Griffin, W.R.; Román-Leshkov, Y. Methane to Acetic Acid over Cu-Exchanged Zeolites: Mechanistic Insights from a Site-Specific Carbonylation Reaction. *J. Am. Chem. Soc.* **2015**, *137*, 1825–1832. [CrossRef]
24. Gao, L.; Zhuang, J.; Nie, L.; Zhang, J.; Zhang, Y.; Gu, N.; Wang, T.; Feng, J.; Yang, D.; Perrett, S.; et al. Intrinsic Peroxidase-like Activity of Ferromagnetic Nanoparticles. *Nat. Nanotechnol.* **2007**, *2*, 577–583. [CrossRef] [PubMed]
25. Kim, S.E.; Zhang, L.; Ma, K.; Riegman, M.; Chen, F.; Ingold, I.; Conrad, M.; Turker, M.Z.; Gao, M.; Jiang, X.; et al. Ultrasmall Nanoparticles Induce Ferroptosis in Nutrient-Deprived Cancer Cells and Suppress Tumour Growth. *Nat. Nanotechnol.* **2016**, *11*, 977–985. [CrossRef]
26. Wu, J.; Wang, X.; Wang, Q.; Lou, Z.; Li, S.; Zhu, Y.; Qin, L.; Wei, H. Nanomaterials with Enzyme-like Characteristics (Nanozymes): Next-Generation Artificial Enzymes (II). *Chem. Soc. Rev.* **2019**, *48*, 1004–1076. [CrossRef] [PubMed]
27. Qiao, B.; Wang, A.; Yang, X.; Allard, L.; Jiang, Z.; Cui, Y.; Liu, J.; Li, J.; Zhang, T. Single-Atom Catalysis of CO Oxidation Using Pt1/FeO*x*. *Nat. Chem.* **2011**, *3*, 634–641. [CrossRef] [PubMed]
28. Gawande, M.B.; Ariga, K.; Yamauchi, Y. Single-Atom Catalysts. *Small* **2021**, *17*, 2101584. [CrossRef] [PubMed]
29. Wang, A.; Li, J.; Zhang, T. Heterogeneous Single-Atom Catalysis. *Nat. Rev. Chem.* **2018**, *2*, 65–81. [CrossRef]
30. Deng, T.; Zheng, W.; Zhang, W. Increasing the Range of Non-Noble-Metal Single-Atom Catalysts. *Chin. J. Catal.* **2017**, *38*, 1489–1497. [CrossRef]
31. Chen, Z.; Yan, J.-M.; Jiang, Q. Single or Double: Which Is the Altar of Atomic Catalysts for Nitrogen Reduction Reaction? *Small Methods* **2018**, *3*, 1800291. [CrossRef]
32. Li, F.; Liu, X.; Chen, Z. $1 + 1' > 2$: Heteronuclear Bi-atom Catalyst Outperforms Its Homonuclear Counterparts for CO Oxidation. *Small Methods* **2019**, *3*, 1800480. [CrossRef]
33. Yan, H.; Lin, Y.; Wu, H.; Zhang, W.; Sun, Z.; Cheng, H.; Liu, W.; Wang, C.; Li, J.; Huang, X.; et al. Bottom-up Precise Synthesis of Stable Platinum Dimers on Graphene. *Nat. Commun.* **2017**, *8*, 1070. [CrossRef] [PubMed]
34. Li, F.; Li, Y.; Zeng, X.C.; Chen, Z. Exploration of High-Performance Single-Atom Catalysts on Support M1/FeO*x* for CO Oxidation via Computational Study. *ACS Catal.* **2015**, *5*, 544–552. [CrossRef]
35. Zhao, J.; Zhao, J.; Li, F.; Chen, Z. Copper Dimer Supported on $C_2N$-Layer as an Efficient Electrocatalyst for $CO_2$ Reduction Reaction: A Computational Study. *J. Phys. Chem. C* **2018**, *122*, 19712–19721. [CrossRef]
36. Abel, M.; Clair, S.; Ourdjini, O.; Mossoyan, M.; Porte, L. Single Layer of Polymeric Fe-Phthalocyanine: An Organometallic Sheet on Metal and Thin Insulating Film. *J. Am. Chem. Soc.* **2011**, *133*, 1203–1205. [CrossRef]
37. Matsushita, O.; Derkacheva, V.M.; Muranaka, A.; Shimizu, S.; Uchiyama, M.; Luk'yanets, E.A.; Kobayashi, N. Rectangular-Shaped Expanded Phthalocyanines with Two Central Metal Atoms. *J. Am. Chem. Soc.* **2012**, *134*, 3411–3418. [CrossRef]
38. Gueorguiev, G.K.; Pacheco, J.M.; Stafström, S.; Hultman, L. Silicon–metal Clusters: Nano-templates for Cluster Assembled Materials. *Thin Solid Films* **2006**, *515*, 1192–1196. [CrossRef]
39. Dos Santos, P.B.; Rivelino, R.; de Brito Mota, F.; Gueorguiev, G.K.; Kakanakova-Georgieva, A. Dopant Species with Al-Si and N-Si Bonding in The MOCVD of AlN Implementing Trimethylaluminum, Ammonia and Silane. *J. Phys. D Appl. Phys.* **2015**, *48*, 295104.
40. Bučko, T.; Hafner, J.; Lebègue, S.; Àngyán, J.G. Improved Description of the Structure of Molecular and Layered Crystals: Ab Initio DFT Calculations with van der Waals Corrections. *J. Phys. Chem. A* **2010**, *114*, 11814–11824. [CrossRef]
41. Blöch, P. Projector Augmented-Wave Method. *Phy. Rev. B* **1994**, *50*, 17953–17979. [CrossRef] [PubMed]
42. Perdew, J.P.; Burke, K.; Ernzerhof, M. Generalized Gradient Approximation Made Simple. *Phys. Rev. Lett.* **1996**, *77*, 3865–3868. [CrossRef]
43. Monkhorst, H.; Pack, J. Special Points for Brillouin-Zone Integrations. *Phys. Rev. B* **1976**, *13*, 5188–5192. [CrossRef]
44. Henkelman, G.; Uberuaga, B.P.; Jónsson, H. A Climbing Image Nudged Elastic Band Method for Finding Saddle Points and Minimum Energy Paths. *J. Chem. Phys.* **2000**, *113*, 9901–9904. [CrossRef]
45. Henkelman, G.; Jónsson, H. Improved Tangent Estimate in the Nudged Elastic Band Method for Finding Minimum Energy Paths and Saddle Points. *J. Chem. Phys.* **2000**, *113*, 9978–9985. [CrossRef]
46. Sangiovanni, D.G.; Gueorguiev, G.K.; Kakanakova-Georgieva, A. Ab initio Molecular Dynamics of Atomic-Scale Surface Rreactions: Insights into Metal Organic Chemical Vapor Deposition of AlN on Graphene. *Phys. Chem. Chem. Phys.* **2018**, *20*, 17751–17761. [CrossRef] [PubMed]
47. Campos-Martin, J.M.; Blanco-Brieva, G.; Fierro, J.L.G. Hydrogen Peroxide Synthesis: An Outlook beyond the Anthraquinone Process. *Angew. Chem. Int. Ed.* **2006**, *45*, 6962–6984. [CrossRef]
48. Sajith, P.K.; Staykov, A.; Yoshida, M.; Shiota, Y.; Yoshizawa, K. Theoretical Study of the Direct Conversion of Methane to Methanol Using $H_2O_2$ as an Oxidant on Pd and Au/Pd Surfaces. *J. Phys. Chem. C* **2020**, *124*, 13231–13239. [CrossRef]
49. Hammond, C.; Forde, M.M.; Ab Rahim, M.H.; Thetford, A.; He, Q.; Jenkins, R.L.; Dimitratos, N.; Lopez-Sanchez, J.A.; Dummer, N.F.; Murphy, D.M.; et al. Direct Catalytic Conversion of Methane to Methanol in an Aqueous Medium by Using Copper-Promoted Fe-ZSM-5. *Angew. Chem. Int. Ed.* **2012**, *51*, 5129–5133. [CrossRef]

50. Ab Rahim, M.H.; Forde, M.M.; Jenkins, R.; Hammond, C.; He, Q.; Dimitratos, N.; Lopez-Sanchez, J.A.; Carley, A.F.; Taylor, S.H.; Willock, D.J.; et al. Oxidation of Methane to Methanol with Hydrogen Peroxide Using Supported Gold-Palladium Alloy Nanoparticles. *Angew. Chem. Int. Ed.* **2013**, *52*, 1280–1284. [CrossRef]
51. Osadchii, D.Y.; Olivos-Suarez, A.L.; Szecsenyi, Á.; Li, G.; Nasalevich, M.A.; Dugulan, L.A.; Crespo, P.S.; Hensen, E.J.M.; Veber, S.L.; Fedin, M.V.; et al. Isolated Fe Sites in Metal Organic Frameworks Catalyze the Direct Conversion of Methane to Methanol. *ACS Catal.* **2018**, *8*, 5542–5548. [CrossRef]
52. Xiao, P.; Wang, Y.; Nishitoba, T.; Kondo, J.N.; Yoko, T. Selective Oxidation of Methane to Methanol with $H_2O_2$ over An Fe-MFI Zeolite Catalyst Using Sulfolane Solvent. *Chem. Commun.* **2019**, *55*, 2896–2899. [CrossRef] [PubMed]
53. Yoo, J.S.; Schumann, J.; Studt, F.; Abild-Pedersen, F.; Nørskov, J.K. Theoretical Investigation of Methane Oxidation on Pd(111) and Other Metallic Surfaces. *J. Phys. Chem. C* **2018**, *122*, 16023–16032. [CrossRef]
54. Dinh, K.T.; Sullivan, M.M.; Serna, P.; Meyer, R.J.; Dincă, M.; Román-Leshkov, Y. Viewpoint on the Partial Oxidation of Methane to Methanol Using Cu- and Fe-Exchanged Zeolites. *ACS Catal.* **2018**, *8*, 8306–8313. [CrossRef]
55. Tsai, C.; Latimer, A.; Yoo, J.S.; Studt, F.; Abild-Pedersen, F. Predicting Promoter-Induced Bond Activation on Solid Catalysts Using Elementary Bond Orders. *J. Phys. Chem. Lett.* **2015**, *6*, 3670–3674. [CrossRef]
56. Yoo, J.S.; Khan, T.S.; Abild-Pedersen, F.; Nørskov, J.K.; Studt, F. On the Role of the Surface Oxygen Species during A–H (A = C, N, O) Bond Activation: A Density Functional Theory Study. *Chem. Commun.* **2015**, *51*, 2621–2624. [CrossRef]
57. Li, J.; Staykov, A.; Ishihara, T.; Yoshizawa, K. Theoretical Study of the Decomposition and Hydrogenation of $H_2O_2$ on Pd and Au@Pd Surfaces: Understanding toward High Selectivity of $H_2O_2$ Synthesis. *J. Phys. Chem. C* **2011**, *115*, 7392–7398. [CrossRef]
58. Serra-Maia, R.; Michel, F.M.; Kang, Y.; Stach, E.A. Decomposition of Hydrogen Peroxide Catalyzed by AuPd Nanocatalysts during Methane Oxidation to Methanol. *ACS Catal.* **2020**, *10*, 5115–5123. [CrossRef]
59. Latimer, A.A.; Aljama, H.; Kakekhani, A.; Yoo, J.S.; Kulkarni, A.; Tsai, C.; Garcia-Melchor, M.; Abild-Pedersen, F.; Nørskov, J.K. Mechanistic Insights into Heterogeneous Methane Activation. *Phys. Chem. Chem. Phys.* **2017**, *19*, 3575–3581. [CrossRef]
60. Latimer, A.A.; Kulkarni, A.R.; Aljama, H.; Montoya, J.H.; Yoo, J.S.; Tsai, C.; Abild-Pedersen, F.; Studt, F.; Nørskov, J.K. Understanding Trends in C–H Bond Activation in Heterogeneous Catalysis. *Nat. Mater.* **2017**, *16*, 225–229. [CrossRef]
61. Fernan, S.; Leonardo, B. Density-Functional Theory Models of Fe(IV)O Reactivity in metal-organic Frameworks: SelfInteraction Error, Spin Delocalisation and The Role of Hybrid Exchange. *Phys. Chem. Chem. Phys.* **2020**, *22*, 12821–12830.
62. Yu, L.; Li, F.; Zhao, J.; Chen, Z. Revisiting Catalytic Performance of Supported Metal Dimers for Oxygen Reduction Reaction via Magnetic Coupling from First Principles. *Adv. Powder Mater.* **2022**, *1*, 100031. [CrossRef]
63. Latimer, A.A.; Kakekhani, A.; Kulkarni, A.; Nørskov, J.K. Direct Methane to Methanol: The Selectivity-Conversion Limit and Design Strategies. *ACS Catal.* **2018**, *8*, 6894–6907. [CrossRef]
64. Da Silva, J.C.S.; Pennifold, R.C.R.; Harvey, J.N.; Rocha, W.R.A. Radical Rebound Mechanism for the Methane Oxidation Reaction Promoted by the Dicopper Center of A pMMO Enzyme: A Computational Perspective. *Dalton Trans.* **2016**, *45*, 2492–2504. [CrossRef]
65. Chin, Y.H.; Buda, C.; Neurock, M.; Iglesia, E. Consequences of Metal-Oxide Interconversion for C–H Bond Activation during CH4 Reactions on Pd Catalysts. *J. Am. Chem. Soc.* **2013**, *135*, 15425–15442. [CrossRef]
66. Bernd, E.; Francesco, B.; Michiel, C.M.G.; Evert, J.B. Methane-to-Methanol Oxidation by the Hydrated Iron(IV) Oxo Species in Aqueous Solution: A Combined DFT and Car-Parrinello Molecular Dynamics Study. *J. Am. Chem. Soc.* **2004**, *126*, 4355–4365.
67. Heyd, J.; Scuseria, G.E.; Ernzerhof, M. Hybrid functionals based on a screened Coulomb potential. *J. Phys. Chem. C* **2003**, *118*, 8207–8215. [CrossRef]